processes

MDPI

Article

The Adsorption of Durene and Prehnitene on Metal–Organic Frameworks

Tianyou Wang, Yanyang Wu *, Jiabo Rao, Xudong Wang, Bin Wu, Kui Chen and Lijun Ji

School of Chemical Engineering, East China University of Science and Technology, Shanghai 200237, China; y30220008@mail.ecust.edu.cn (T.W.); y30210100@mail.ecust.edu.cn (J.R.); y30220077@mail.ecust.edu.cn (X.W.); wubin@ecust.edu.cn (B.W.); chenkui@ecust.edu.cn (K.C.); jilijun@ecust.edu.cn (L.J.)
* Correspondence: wyywitty@ecust.edu.cn

Abstract: Tetratoluene has the following three isomers: durene (DR), prehnitene (PR), and isodurene (IR). DR and PR often coexist during the separation of C10 heavy aromatics at different levels. They are both important organic chemical raw materials and their separation is the key to the high-efficiency industrial utilization of C10 heavy aromatics. In this paper, six metal–organic frameworks (MOFs), including ZU-61, MIL-101, UIO-66, UIO-66-NH_2, Mg-MOF-74, and MIL-53(Al), were used as the adsorbents of DR and PR. Their skeletons were structurally optimized using VASP software (latest v. 6.4.3). The adsorption capacity and isosteric heats of both pure components and mixtures (the molar ratio was 1:1) in gas were calculated using Grand Canonical Monte Carlo simulation from 10 kPa to 300 kPa at 298 K. The results indicated that all adsorption processes were physical. ZU-61, UIO-66, UIO-66-NH_2, and Mg-MOF-74 presented suitable capacity differences for DR and PR at 300 kPa. The selectivity values of these frameworks were all above 1.5. Thus, the four MOFs were prepared using the solvothermal method and characterized by SEM and XRD. Then, the competitive adsorption of DR and PR in liquid on the four MOFs was carried out as well. The results showed good agreement with the simulation in general, with a lower adsorption attained capacity due to the different phase states of both DR and PR. This study can guide the separation of tetratoluene isomers in C10 heavy aromatics.

Keywords: metal–organic frameworks; durene; prehnitene; simulation; adsorption

check for updates

Citation: Wang, T.; Wu, Y.; Rao, J.; Wang, X.; Wu, B.; Chen, K.; Ji, L. The Adsorption of Durene and Prehnitene on Metal–Organic Frameworks. *Processes* **2024**, *12*, 2331. https://doi.org/10.3390/pr12112331

Received: 24 September 2024
Revised: 14 October 2024
Accepted: 23 October 2024
Published: 24 October 2024

Copyright: © 2024 by the authors. Licensee MDPI, Basel, Switzerland. This article is an open access article distributed under the terms and conditions of the Creative Commons Attribution (CC BY) license (https://creativecommons.org/licenses/by/4.0/).

1. Introduction

In recent years, C10 heavy aromatics have gained a great deal of attention with the development of the coal chemical and petrochemical industries. An appreciable amount of tetratoluene exists in C10 heavy aromatics [1]. It involves three isomers: durene (DR), prehnitene (PR), and isodurene (IR). The isomers mainly contain DR and PR, and the content of IR is relatively low during enrichment [2]. Meanwhile, DR is widely used in fields such as machinery [3,4], aerospace [5,6], nanotechnology [7,8], and membrane separation [9–11]. PR can also play an important role in various fields such as machinery [12], electronics [12,13], and aerospace [14]. The separation of DR and PR is difficult due to their similar properties, which restricts the efficient utilization of C10 heavy aromatics [15].

In this paper, UIO-66, UIO-66-NH_2, Mg-MOF-74, ZU-61, MIL-101, and Al-MIL-53 were preliminary selected as adsorbents for use in the separation of DR and PR according to the insights of our previous research. The adsorption isotherms and isosteric heats of both pure components and mixture were calculated via Grand Canonical Monte Carlo (GCMC) simulation using Materials Studio 2019. MOFs with high selectivity were prepared by the solvothermal method and characterized via X-ray diffraction (XRD) and scanning electron microscopy (SEM). Subsequently, their adsorption behavior towards DR and PR was investigated.

2. Literature Review

At present, the main reported separation methods for DR and PR are extractive distillation [16,17], melt crystallization [18,19], and recrystallization [20]. In general, DR is first concentrated via extraction distillation. Then, DR with a purity between 93% and 95% is obtained via melt crystallization at around 253.15 K [21–23]. Recrystallization is normally carried out for further purification. Li et al. [24] used ethanol as a solvent for recrystallization purification. They investigated crystallization conditions and finally increased the purity of DR to 99%. However, there is still a long way to go before the industrial separation of DR and PR due to the large investment required, the low yield of DR, and the complicated separation process [25].

Adsorption can be a promising method for the separation of DR and PR. It draws a lot of attention, especially in the search for a new and structurally designed adsorbent [26]. Metal–organic frameworks (MOFs) are a type of three-dimensional crystalline material combined with metal clusters and organic linkers [27]. They are highly recommended as adsorbents due to their strong stability [28,29], large porous volumes [30,31], high specific surface areas [32], and adjustability due to flexible structures [33,34]. MOFs have been widely applied in the adsorption of aromatic isomers. Many studies focus on the separation of xylene isomers [35,36]. MIL-120(Al) showed high selectivity values of 11.5 and 8.3 for p-xylene/o-xylene and p-xylene/m-xylene, respectively [37]. The selectivity of o-xylene/m-xylene on MIL-68(Al) was 8.1 [38]. Yang [39] found that anion-pillared MOF SIFSIX-1-Cu showed strong affinity with m-xylene via a competition adsorption experiment involving p-xylene and m-xylene. We obtained p-xylene with a purity of 99% after adsorption and the subsequent processes.

In the meantime, the adsorption mechanism has been investigated via molecular simulation [40]. Kim et al. [41] investigated the adsorption mechanism of p-xylene towards DUT-8 using GCMC simulation and Density Functional Theory (DFT). The results showed that the presence of the DABCO ligand was responsible for the preferential adsorption of p-xylene due to the packing of molecules. Ji et al. [42] found that the adsorption capacity and heat of m-xylene were significantly smaller than those of p-xylene and o-xylene on Cu-HKUST-1, which could be a suitable adsorbent for xylene isomers.

3. Methodology and Analysis

3.1. Simulation

3.1.1. Structure Optimization

The crystal structures of MOFs were downloaded from the Cambridge Crystal Data Centre (CCDC). The MOFs' structures were optimized and then DDEC charges were calculated using the Vienna Ab initio Simulation Package (VASP) [43,44]. In the meantime, the structures of DR and PR were optimized, with the objective of using a minimum amount of energy for the system. This was performed via the Universal Force Field (UFF) in Materials Studio 2019 using the Forcite module [45]. Energy, force, and displacement converged to within 10^{-4} kcal/mol, 0.005 kcal/(mol·Å), and 5×10^{-5} Å, respectively. In the optimization, long-range electrostatic and van der Waals interactions were calculated via an atom-based summation method [46].

3.1.2. Simulation Methods

GCMC simulation was performed with the sorption module in Materials Studio 2019. The skeletons of MOFs were expanded to $2 \times 2 \times 1$ supercells and kept rigid during the simulation to satisfy the periodic boundary conditions [47,48]. Adsorption isotherms and isosteric heats of both pure components and mixtures in gas were calculated from 10 kPa to 300 kPa at 298 K using the configurational bias sampling method. The partial pressure of DR or PR in a mixture was related to the fugacity, which was calculated via the Peng–Robinson equation [49]. It varied from 5 kPa to 150 kPa. The insertion, rotation, deletion, and movement of adsorbates had the same probability of occurring throughout

the calculations [50]. A total of 2×10^6 steps was set. The first 10^6 steps were used to reach equilibrium, while the last ones were for production.

Established based on previous empirical parameters and experimental data, a force field is a collection of functional formulas or parameters. In this study, all atoms of adsorbents and adsorbates were described via the commonly used universal force field (UFF), which can be used to describe the interaction between organic materials. Long-range electrostatic interactions were described via the Ewald summation method [51], where the Ewald accuracy and cutoff distance were 0.001 kcal/mol and 12.5 Å, respectively. The van der Waals interactions were calculated by an atom-based summation method [52]. Truncation, cutoff distance, and spline width were a cubic spline, 12.5 Å, and 1 Å, respectively. The interaction potential E_{ij} was calculated using a Lennard-Jones (LJ) potential function with a Lorentz–Berthelot mixing rule [53]. Relevant functions are shown in Equations (1)–(3). LJ parameters were taken from Materials Studio 2019 and are listed in Table 1.

$$E_{ij} = 4\varepsilon_{ij}\left[\left(\frac{\sigma_{ij}}{r_{ij}}\right)^{12} - \left(\frac{\sigma_{ij}}{r_{ij}}\right)^{6}\right] + \frac{q_i q_j}{4\pi\varepsilon_0 r_{ij}} \quad (1)$$

$$\varepsilon_{ij} = \sqrt{\varepsilon_i \varepsilon_j} \quad (2)$$

$$\sigma_{ij} = \frac{1}{2}(\sigma_i + \sigma_j) \quad (3)$$

where r_{ij} (Å) is the distance between particles i and j; ε (kcal/mol) is the potential well depth; σ (Å) is the intermolecular radius when the potential energy function is 0; q (e) is the atomic charge; and ε_0 (F/m) is the dielectric constant at vacuum conditions.

Table 1. Lennard-Jones parameters.

Atom Type	LJ Parameters	Atom Type									
		C_j	H_j	N_j	O_j	Zr_j	F_j	Ni_j	Mg_j	Al_j	Cr_j
C_i	ε (kcal/mol)	0.105	0.068	0.085	0.072	0.085	0.072	0.040	0.108	0.230	0.040
	σ (Å)	3.851	3.369	3.756	3.676	3.488	3.608	3.343	3.436	4.175	3.437
H_i	ε (kcal/mol)	0.068	0.044	0.055	0.051	0.055	0.047	0.026	0.070	0.149	0.026
	σ (Å)	3.369	2.886	3.273	3.193	3.005	3.125	2.860	2.954	3.693	2.955

i for DR (or PR) and j for MOFs.

The adsorption capacity calculated via GCMC simulation was always the absolute adsorption capacity, while that measured by the experiment was the excess adsorption capacity [53]. The conversion of the two kinds of capacity was calculated as follows:

$$N^{ex} = N^{abs} - V^g \rho^g \quad (4)$$

where N^{ex} is the excess adsorption capacity; N^{abs} is the absolute adsorption capacity; V^g (cm^3/g) is the pore volume of the adsorbent; and ρ^g (g/cm^3) is the density of adsorbate obtained using the Peng–Robinson equation.

3.1.3. Adsorption Heat

Some energy was released as isosteric heat of adsorption Q_{st} when an adsorbate was adsorbed on MOFs. It could be calculated using GCMC simulation via Equation (5) [54].

$$Q_{st} = \frac{\langle U\rangle\langle n\rangle - \langle Un\rangle}{\langle n^2\rangle - \langle n\rangle^2} + k_B T \quad (5)$$

where the brackets represent the ensemble average; U (kJ/mol) is the potential energy; n is the number of adsorbate molecules; k_B (J/K) is the Boltzmann constant; and T (K) is temperature.

3.2. Experiment

3.2.1. Synthesis

In this paper, UIO-66, UIO-66-NH_2, ZU-61, and Mg-MOF-74 were prepared via the solvothermal method.

UIO-66

We added 190.3 mg of $ZrCl_4$, 133 mg of 1,4-dicarboxybenzene (BDC), and 5.4 g of HCl into 81.7 mL of N,N-dimethylformamide (DMF) in sequence. The solution was stirred magnetically for 2 h. This was followed by ultrasonic treatment for 20 min. Then, it was poured into a high-pressure hydrothermal reactor lined with polytetrafluoroethylene and heated at 393 K for 24 h. After cooling to room temperature, the solid product was obtained by centrifugation. It was washed with methanol and DMF three times, respectively. The product was obtained after being dried overnight at 333 K [17].

UIO-66-NH_2

The solution including 2-amino-BDC, $ZrCl_4$, HCl, and DMF was prepared at a certain molar ratio (2:2:1:76) under magnetic stirring. It was transferred to a high-pressure hydrothermal reactor lined with polytetrafluoroethylene and reacted at 453 K for 24 h. After cooling to room temperature, the solution was centrifuged at 6000 r/min. The solid was washed with ethanol and DMF three times, respectively. Product was obtained after being vacuum-dried at 363 K [55].

ZU-61

We added 0.74 g of NiO and 1.584 g of Nb_2O_5 to 5 mL of HF (48–50%), respectively. The mixed solution was poured into a high-pressure hydrothermal reactor lined with polytetrafluoroethylene and reacted at 413 K for 24 h to obtain $NiNbOF_5$. Then, 0.41 g of $NiNbOF_5$ was added to 20 mL of H_2O and 0.35 g of 4,4-bipyridine was added to 40 mL of ethylene glycol. The two solutions were mixed together and then stirred at 338 K for 1 h. The mixture was soaked in methanol for 24 h. The product was obtained after centrifugation [56].

Mg-MOF-74

We added 0.6432 g of $MgNO_3{\cdot}4H_2O$, 0.2972 g of 2,5-dihydroxy-BDC, and 2 mL of deionized water to 18 mL of N-Methyl-2-pyrrolidone, respectively. The solution was stirred for 30 min and poured into a high-pressure hydrothermal reactor at 393 K for 24 h. It was washed with N-Methyl-2-pyrrolidone 3 times and soaked in methanol for 4 days. The target product was prepared after drying the solids in a vacuum-drying oven at 423 K for 6 h, followed by centrifugation [57].

3.2.2. Batch Adsorption

The batch adsorption of DR and PR (molar ratio was 1:1) on UIO-66, UIO-66-NH_2, ZU-61, and Mg-MOF-74, respectively, was carried out at 298 K under stirring. A certain number of MOFs were added into the solution, with n-hexane acting as the solvent. After adsorption, samples were analyzed by high-performance liquid chromatography. The adsorption of each material was assessed three times for accuracy. The adsorption capacity of DR or PR is calculated as follows:

$$Q_t = \frac{(C_0 - C_t) \times m_1}{m_2} \quad (6)$$

where Q_t (mg/g) is the adsorption capacity; C_0 and C_t (mg/g) are the mass concentrations of DR or PR before and after adsorption; m_1 (g) is the mass of solution; and m_2 (g) is the mass of adsorbent [58].

3.2.3. Selectivity

Selectivity α is an important parameter in adsorption. It reflects the separation ability of MOFs. Higher selectivity leads to a stronger ability to separate one component from a mixture. The adsorption of each material was repeated three times for accuracy. The selectivity can be calculated as follows:

$$\alpha = \frac{y_1/y_2}{x_1/x_2} \quad (7)$$

where y_1 and y_2 (mg/g) are the adsorption capacity of components 1 and 2 (the component with a higher adsorption capacity is designated as component 1) and x_1/x_2 are the molar ratios of two components before adsorption [59].

3.2.4. Regeneration

After adsorption, ZU-61 was centrifuged and then washed with methanol for 4 h, which was repeated 3 times. Afterwards, the adsorbent was dried in a vacuum oven at 333 K for 8 h. Then, it was used for the next adsorption. This process was repeated for 5 cycles.

4. Results and Discussion

4.1. Validation of Force Field Parameters

To verify the accuracy of the force field used in this study, we calculated the adsorption isotherm of CH_4 on Mg-MOF-74 via GCMC simulation. Then, the result was compared with the reported experimental data [60]. This comparison is shown in Figure 1. It is evident that the simulation result was consistent with the experimental data. So, the force field used in this study was effective and accurate.

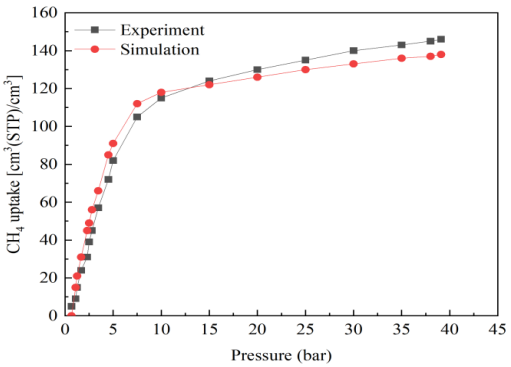

Figure 1. The validation of the CH_4 adsorption field using Mg-MOF-74.

4.2. Structure

The structures of DR and PR after optimization are shown in Figure 2. The optimized crystalline structures of MOFs are shown in Figure S1.

The atomic charges of DR and PR were calculated by the QEq method and all charges are listed in Table S1. The calculated values presented symmetry, which could be explained by the fact that the molecular structures of both DR and PR were symmetrical. For convenience, the minimum symmetry units were classified and their charges are listed in Table 2. There were 5 atoms in the minimum unit of DR and 8 atoms in that of PR.

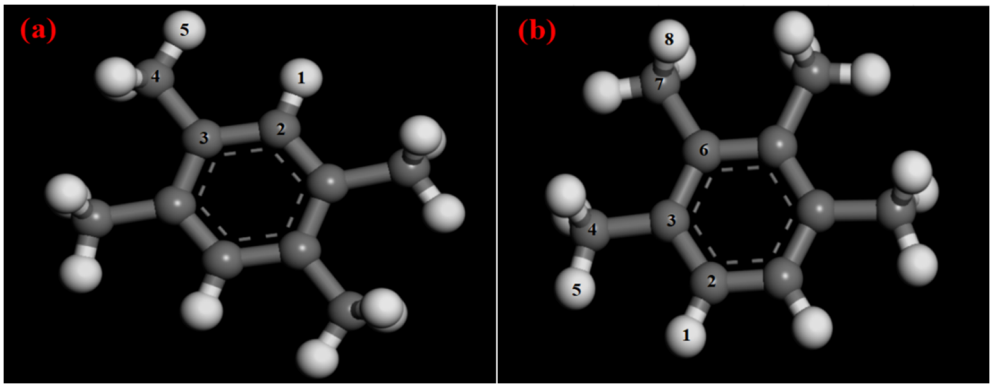

Figure 2. Optimized structures of tetratoluene: (**a**) DR; (**b**) PR.

Table 2. Atomic charges of DR and PR.

	Charges/e							
	1	**2**	**3**	**4**	**5**	**6**	**7**	**8**
DR	0.0938	−0.0962	0.0334	−0.4018	0.1223	-	-	-
PR	0.0959	−0.1104	0.0341	−0.4023	0.1212	0.0462	−0.3972	0.1170

4.3. Adsorption of Pure Components

4.3.1. Isotherms of DR

The adsorption isotherms of pure DR at 298 K are shown in Figure 3. Its adsorption capacity on all MOFs increased with increasing pressure and approximately reached equilibrium at 300 kPa. Al-MIL-53 presented the biggest adsorption capacity of 414.89 mg/g, while UIO-66-NH_2 showed the smallest capacity of 83.96 mg/g at equilibrium. This could be attributed to the larger surface area and pore volume of Al-MIL-53 compared to the smaller values of UIO-66-NH_2 [28,55]. The adsorption isotherms of DR on both UIO-66 and Mg-MOF-74 showed similar trends. The adsorption capacity increased from 60.58 mg/g and 50.14 mg/g to 190.38 mg/g and 160.67 mg/g, respectively. Big variations in adsorption capacity were observed for both ZU-61 and MIL-101, with increases of 222.94 mg/g and 281.43 mg/g, respectively. This could be explained by their flexible skeletons, which vary, after which the pore volume increases as pressure rises [56,61].

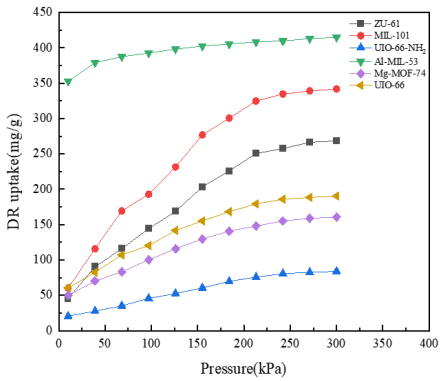

Figure 3. Adsorption isotherms of DR at 298 K.

At pressures no greater than 30 kPa, the adsorption capacity of DR presented a decreasing order: Al-MIL-53 > UIO-66 > MIL-101 > Mg-MOF-74 > ZU-61 > UIO-66-NH_2. However, at the range of 30–300 kPa, the order changed to the following: Al-MIL-53 > MIL-101 > ZU-61 > UIO-66 > Mg-MOF-74 > UIO-66-NH_2. Obviously, the adsorption capacity of UIO-66-NH_2 was less than that of UIO-66. It might be due to the introduction of

amino groups, improving spatial hindrance and thus reducing the affinity of DR towards MOFs [62].

4.3.2. Isotherms of PR

The adsorption isotherms of PR are shown in Figure 4. PR presented a similar tendency to DR. The adsorption capacity increased rapidly from 10 to 200 kPa and gradually reached equilibrium at the range of 200–300 kPa. For PR, similar to the isomers of DR, Al-MIL-53 presented the biggest adsorption capacity at 415.28 mg/g while UIO-66-NH_2 presented the smallest at 63.19 mg/g. ZU-61 and MIL-101 showed similar performances, and their isotherms intersected at around 180 kPa. ZU-61 presented greater capacity when pressure increased from 10 to 180 kPa, while MIL-101 performed better when pressure was in the range of 180–300 kPa. This could be explained by the 'breathe' effect of the MIL-101 skeleton. The increasing pressure increased pore volume, which led to the adsorption capacity increasing faster than that of ZU-61 [63].

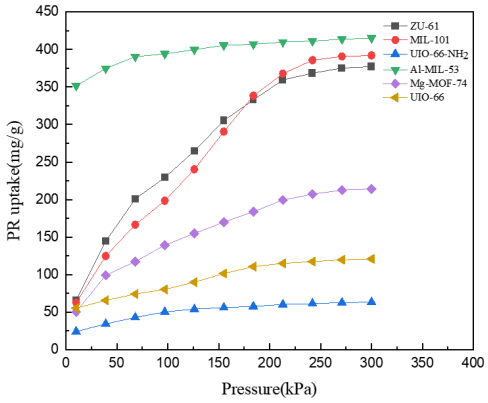

Figure 4. Adsorption isotherms of PR at 298 K.

4.3.3. Adsorption Heats of Pure Components

The isosteric heats of DR and PR on MOFs from 10 kPa to 300 kPa at 298 K are shown in Figure 5. All the isosteric heats of DR or PR fell in the range of 17–32 kJ/mol. ZU-61, Al-MIL-53, and UIO-66 presented higher isosteric heats. In general, the isosteric heats of the other three MOFs could be listed in the following order: UIO-66-NH_2 > Mg-MOF-74 > MIL-101. In addition, the adsorption heat of DR on UIO-66-NH_2 showed maximum variation from 18.68 kJ/mol to 28.30 kJ/mol.

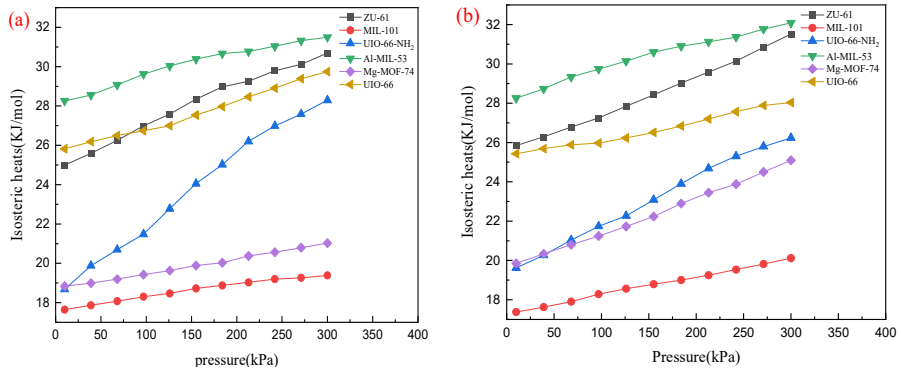

Figure 5. Isosteric heats for different MOFs at 298 K: (**a**) DR; (**b**) PR.

A higher isosteric heat was released when the interaction between the adsorbate and adsobent became stronger. Thus, isosteric heat reflected the interaction between adsorbate and adsorbent [64]. The highest isosteric heat on Al-MIL-53 meant the strongest

adsorbate–adsorbent interaction, which provides a reasonable explanation for it having the highest capacity.

In the meantime, the isosteric heat can be used to classify the adsorption process as either physical or chemical. It is physical when isosteric heat is < 40 kJ/mol, but chemical when isosteric heat is >80 kJ/mol [65]. Therefore, the adsorption processes on six MOFs were all physical.

4.4. Adsorption of Mixture

4.4.1. Isotherms of Mixture

The adsorption capacities of DR and PR on six MOFs at 300 kPa are listed in Table 3. Capacity differences were calculated accordingly. ZU-61, Mg-MOF-74, UIO-66, and UIO-66-NH_2 presented different performances for DR and PR. The adsorption capacity of PR was higher than that of DR on ZU-61 and Mg-MOF-74, while the adsorption capacity of DR was higher than that of PR on UIO-66 and UIO-66-NH_2, which reflects the different affinity of DR and PR towards MOFs. Their selectivity values were all above 1.5 and can be listed in a decreasing order as follows: ZU-61 > UIO-66 > Mg-MOF-74 > UIO-66-NH_2. Al-MIL-53 showed a big adsorption capacity but low selectivity. Meanwhile, MIL-101 presented the lowest selectivity among all the six MOFs. This meant that the separation of DR and PR by Al-MIL-53 or MIL-101 was hard to perform. So, this paper further selected ZU-61, Mg-MOF-74, UIO-66, and UIO-66-NH_2 to simulate the adsorption of mixtures.

Table 3. The adsorption capacity of a mixture on six MOFs at 300 kPa.

	ZU-61		**MIL-101**		**UIO-66-NH_2**		**Al-MIL-53**		**Mg-MOF-74**		**UIO-66**	
Capacity (mg/g)	DR 110.85	PR 261.39	DR 196.20	PR 204.05	DR 80.03	PR 48.38	DR 241.48	PR 324.58	DR 100.14	PR 176.67	DR 158.81	PR 83.44
Capacity difference (mg/g)	150.54		7.85		31.65		83.10		76.53		75.37	
α	2.36		1.04		1.65		1.34		1.76		1.90	

The adsorption capacity and selectivity of DR and PR on ZU-61, Mg-MOF-74, UIO-66, and UIO-66-NH_2, at pressures ranging from 10 kPa to 300 kPa, were calculated according to the information above. The results are shown in Figure 6.

The selectivity values of PR/DR on both ZU-61 and Mg-MOF-74 were greater than 1 and increased with the increase in pressure from 10 to 200 kPa. They were then maintained at around 2.35 and 1.73, respectively. ZU-61 presented larger adsorption capacities of 261.39 mg/g and 110.85 mg/g for PR and DR at 300 kPa, respectively, which might be attributed to the pillar anion that can form a synergetic H bond and provide possible adsorption sites [66]. Meanwhile, the square structure of ZU-61 underwent deformation during adsorption and the pillar anion $NbOF_5^{2-}$ rotated to fit the different shapes of isomers. This self-adjustment property enabled the discrimination of isomers with subtle differences [61,66]. Then, the variations in the adsorption capacity of PR and DR on ZU-61 were bigger than those on Mg-MOF-74, with increases of 201.15 mg/g and 77.57 mg/g from 10 kPa to 300 kPa, respectively. The adsorption capacity of DR on Mg-MOF-74 was similar to that on ZU-61 while the adsorption capacity of PR on Mg-MOF-74 was much lower than that on ZU-61, especially at high pressures. So, the selectivity of PR/DR on Mg-MOF-74 was lower than that on ZU-61.

On the contrary, UIO-66 and its functionalized MOF UIO-66-NH_2 presented high selectivity values of DR/PR that were greater than 1. Their selectivity changed little and remained at around 1.88 and 1.60 with the increase in pressure, which meant that the increasing rates of the adsorption capacity of DR on two MOFs were similar to those of PR. The adsorption capacities of DR and PR on UIO-66-NH_2 reached 80.03 mg/g and 48.38 mg/g at 300 kPa, which were smaller than those of the other three MOFs. The molecular dynamics diameters of both DR and PR were higher than the pore diameter of

UIO-66-NH_2. Most molecules adhered to the surface rather than the inner pore during adsorption. This could explain its low capacity, similar for both DR and PR, which became one of the reasons for its relatively low selectivity [67]. UIO-66 showed a higher adsorption capacity than UIO-66-NH_2, which could be explained by the bigger surface area and pore volume. The adsorption capacity of DR and PR on UIO-66 increased from 57.78 mg/g and 31.03 mg/g to 158.81 mg/g and 83.44 mg/g, respectively.

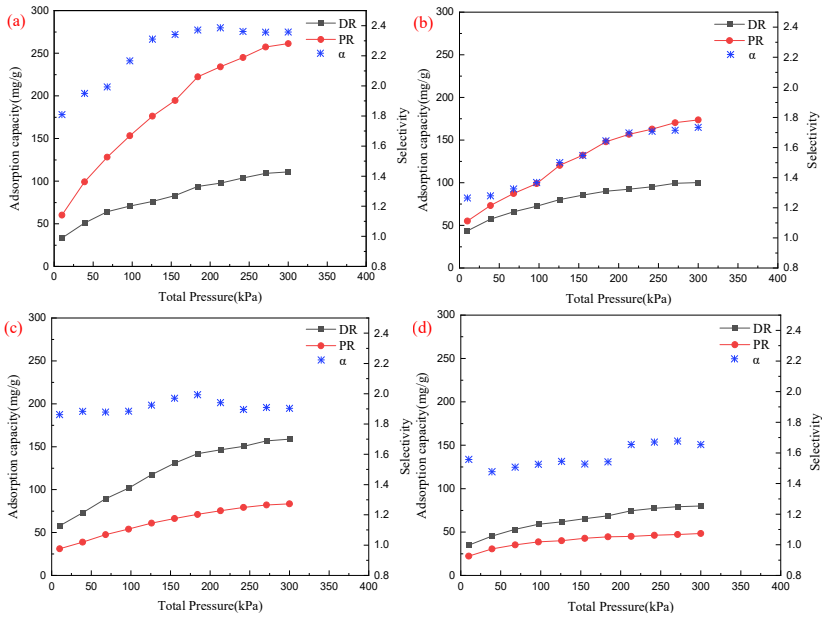

Figure 6. Adsorption capacity and selectivity from 10 kPa to 300 kPa: (**a**) ZU-61; (**b**) Mg-MOF-74; (**c**) UIO-66; (**d**) UIO-66-NH_2.

According to the above, ZU-61 presented the highest selectivity and largest capacity in the adsorption of DR and PR. The structure of ZU-61 was optimized by VASP software in order to understand the adsorption mechanism of ZU-61. As shown in Figure S1, (a) ZU-61 consisted of 4,4′-bipyridine and the rotational ligand $NbOF_5^{2-}$, which were alternately connected and then formed a square pore space. The anion pillar $NbOF_5^{2-}$ provided accessible Lewis basic sites, which served as adsorption sites. The electrostatic potentials of DR and PR are shown in Figure 7. The adjacent methyl groups at the benzene ring of PR shower stronger electron acceptability than DR, which indicated that PR bound to anion pillars more easily than DR. The ionic strength could also affect the adsorption, which is more pronounced with stronger polarity. This effect could be explained by the enhancement of the polar interactions in combination with the salting-out effect [68].

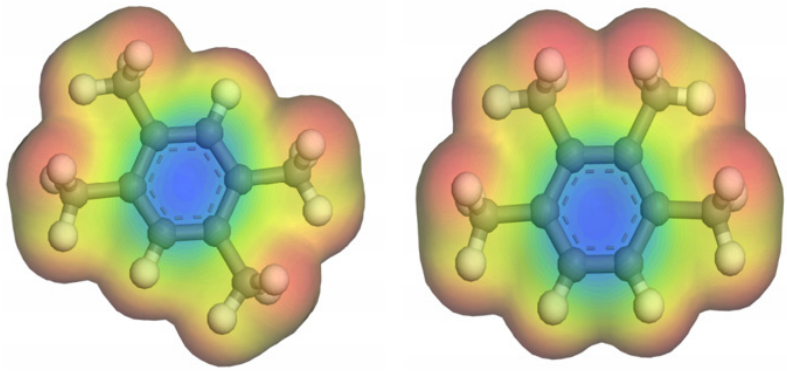

Figure 7. Molecular electron density of DR and PR.

4.4.2. Adsorption Heats of Mixture

The isosteric heats of DR and PR in mixtures were calculated at pressures ranging from 10 kPa to 300 kPa, as shown in Figure 8. The adsorption heats of DR and PR on the four MOFs all increased with the increasing pressure. The isosteric heats and thus the interactions between DR (or PR) and MOFs followed a decreasing order: ZU-61 > UIO-66 > UIO-66-NH_2 > Mg-MOF-74.

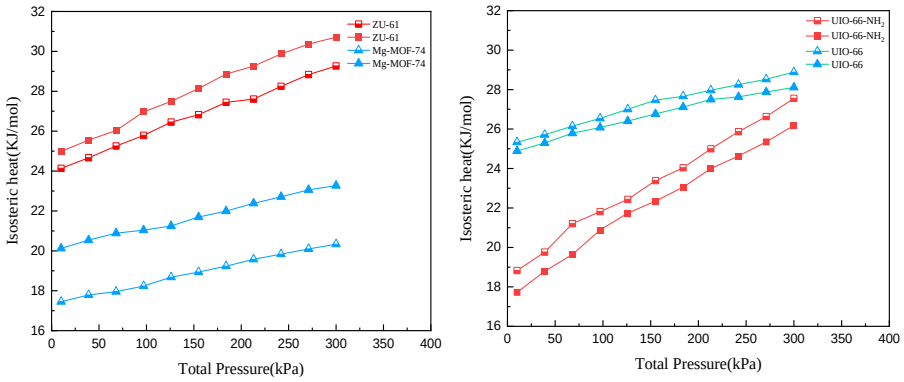

Figure 8. Isosteric heats of DR (hollow data points) and PR (solid data points) from 10 kPa to 300 kPa.

According to Figure 8, ZU-61 and Mg-MOF-74 presented higher isosteric heats for PR than for DR, while UIO-66 and UIO-66-NH_2 presented higher isosteric heats for DR than for PR. This could explain the capacity differences between DR and PR in mixture. Meanwhile, the heat differences between DR and PR on ZU-61 and Mg-MOF-74 were bigger than those on UIO-66 and UIO-66-NH_2, which showed agreement with the results of capacity differences on four MOFs.

4.5. Experimental Results

The four MOFs of UIO-66, UIO-66-NH_2, Mg-MOF-74, and ZU-61 were prepared via the solvothermal method and characterized by XRD and SEM. The results are shown in Figures 9–12 and were consistent with those in the simulation and the literature [17,55–57]. The major diffraction peaks were sharp, and no characteristic peaks of impurity were observed. The pore sizes of four MOFs were distributed around 0.72 nm, 0.66 nm, 0.91 nm, and 0.85 nm, respectively (Figure S3). The competitive adsorption performances of DR and PR on UIO-66, UIO-66-NH_2, Mg-MOF-74, and ZU-61 are listed in Table 4.

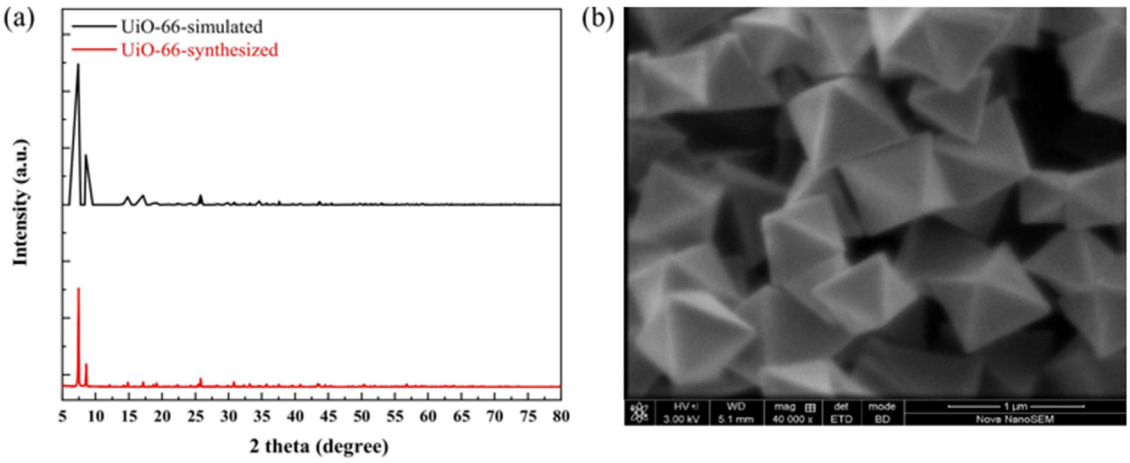

Figure 9. The characterization of UIO-66: (**a**) XRD; (**b**) SEM.

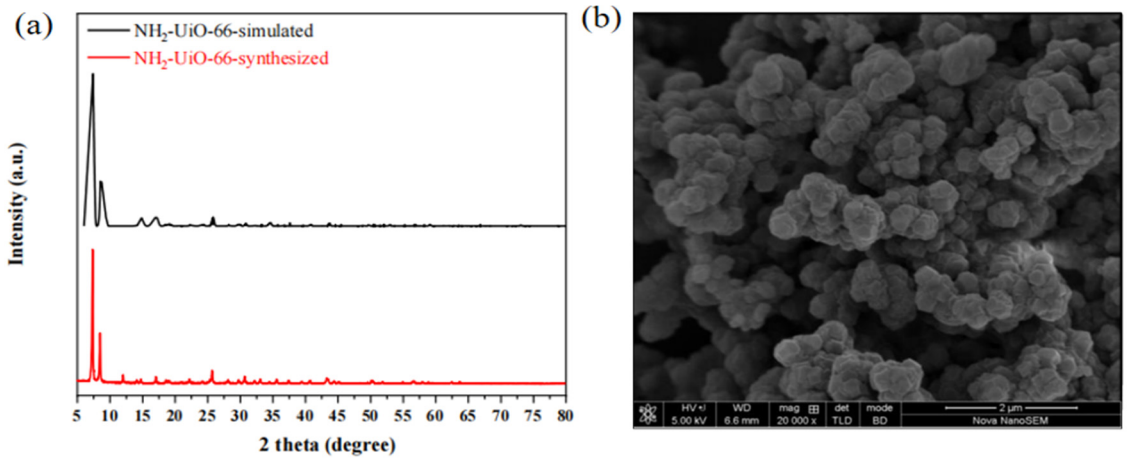

Figure 10. The characterization of UIO-66-NH_2: (**a**) XRD; (**b**) SEM.

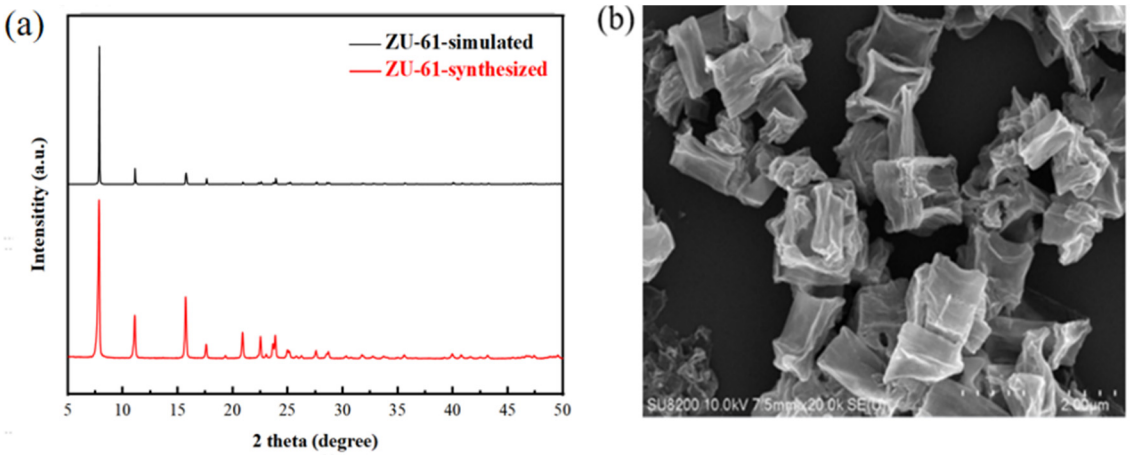

Figure 11. The characterization of ZU-61: (**a**) XRD; (**b**) SEM.

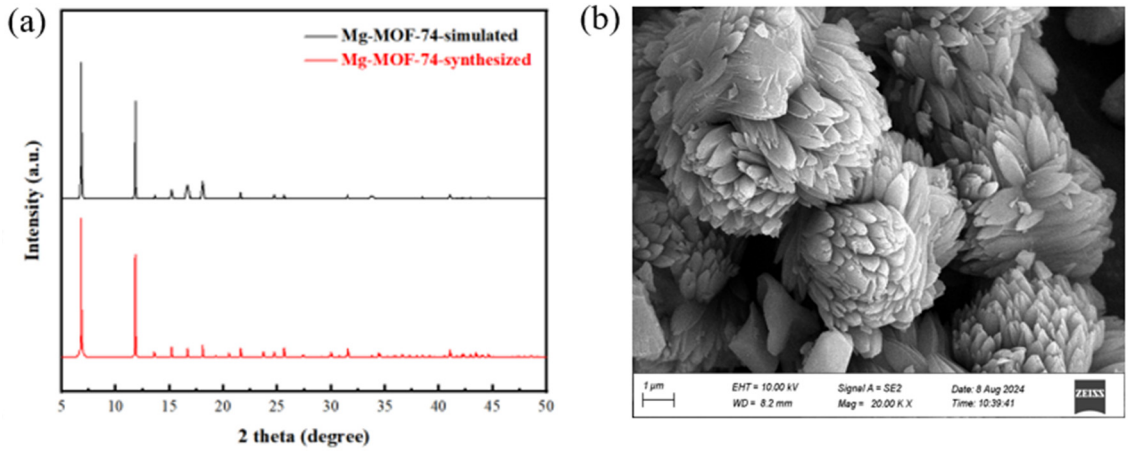

Figure 12. The characterization of Mg-MOF-74: (**a**) XRD; (**b**) SEM.

Table 4. Adsorption capacity of DR and PR on the four MOFs.

MOFs	UIO-66	UIO-66-NH_2	ZU-61	Mg-MOF-74
Adsorption capacity of DR (mg/g)	146.27	70.58	103.75	95.82
Adsorption capacity of PR (mg/g)	79.49	44.39	239.66	165.77
α	1.84	1.59	2.31	1.73
n	3	3	3	3
SD of DR	0.17	0.15	0.21	0.16
SD of PR	0.20	0.09	0.08	0.22

UIO-66 and UIO-66-NH_2 shower a bigger capacity for DR than PR. This was contrary to the values obtained for ZU-61 and Mg-MOF-74, which were consistent with the simulation result. Among the four MOFs, ZU-61 presented the best performance while UIO-66 and Mg-MOF-74 fell in the middle regarding both the adsorption capacity and selectivity. UIO-66-NH_2 showed a lower adsorption capacity for both DR and PR, with a H atom on a benzene ring being modified by -NH_2. This might be explained by the presence of -NH_2, increasing the spatial hindrance and then reducing the pore volume and specific surface area [62].

Compared with the values in Tables 3 and 4, the experimental results presented good agreement with the simulation in general, with lower capacity and selectivity than the simulation values. This could be explained by the following reasons. (1) The simulation proceeded using gas. According to the section addressing the validation of force field parameters, the values calculated using the method in this paper were quite close to the experimental data relating to gas adsorption found in the literature. In general, the adsorption application of MOFs in industry is utilized in the liquid phase, but there is no liquid phase simulation method. So, DR and PR were adsorbed as liquids in the experiments but treated as gases in the simulation, where the rate of mass transfer was faster than that seen in the experiments. Thus, the adsorption capacity and selectivity in simulation were higher than those in experiments [69,70]. (2) In the simulation, the adsorption capacity of MOFs was calculated at 300 kPa, while the adsorption experiments proceeded at atmospheric pressures rather than at high pressures and temperatures. (3) The experimentally synthesized MOFs might contain small defects, which would result in a decrease in pore volume compared to the ideal model used in the simulation.

Regeneration is important for industrial applications. The adsorption performances of ZU-61 for both PR and DR were investigated for five cycles. As shown in Figure 13, adsorption capacity of both PR and DR gradually decreased and then leveled off as the number of cycles increased. In the fifth cycle, the adsorption amount was 96% of that seen in the first cycle, and the selectivity of PR/DR on ZU-61 changed little during regeneration. This indicated that ZU-61 had good recycling performances and practical applicability.

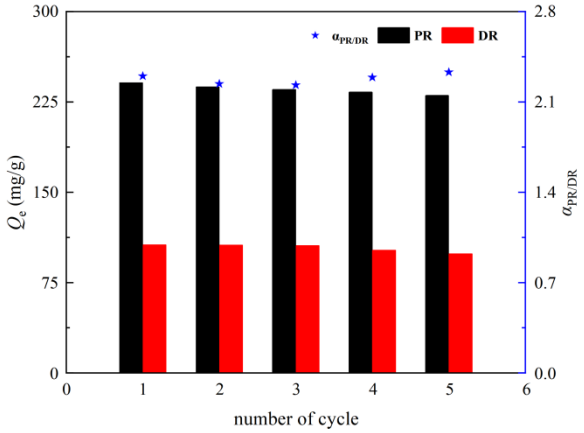

Figure 13. Effects of cycle numbers on the adsorption capacity of PR and DR.

5. Conclusions Implications and Future Works

The adsorption of DR and PR on the MOFs, including UIO-66, UIO-66-NH_2, ZU-61, Mg-MOF-74, Al-MIL-53, and MIL-101, was studied by simulation and experiments in this paper. The adsorption capacity and isosteric heats of both pure components and mixtures from 10 kPa to 300 kPa at 298 K were calculated via GCMC simulation. The adsorption capacity of both DR and PR increased with increasing pressure. All isosteric heats were <40 kJ/mol, which meant that all processes were physical. For mixtures (where the molar ratio was 1), the adsorption capacity values of DR on UIO-66, UIO-66-NH_2, ZU-61, and Mg-MOF-74 at 300 kPa were 158.81 mg/g, 80.03 mg/g, 110.85 mg/g, and 100.14 mg/g, respectively, while those of PR were 83.44 mg/g, 48.38 mg/g, 261.39 mg/g, and 176.67 mg/g, respectively. The selectivity of the four MOFs could reach 1.90, 1.65, 2.36, and 1.76, respectively.

The four MOFs of ZU-61, Mg-MOF-74, UIO-66, and UIO-66-NH_2 were prepared solvothermally and characterized by SEM and XRD. The results were inconsistent with the literature and simulation. Competitive adsorption experiments of DR and PR were further carried out on UIO-66, UIO-66-NH_2, ZU-61, and Mg-MOF-74 at 298 K. The adsorption capacities of DR were 146.27 mg/g, 70.58 mg/g, 103.75 mg/g, and 95.82 mg/g, respectively, while those of PR were 79.49 mg/g, 44.39 mg/g, 239.66 mg/g, and 165.77 mg/g, respectively. Their selectivity values were 1.84, 1.59, 2.31, and 1.73. The experimental results showed good agreement with the simulation in general, with lower adsorption capacity and selectivity. This could mainly be attributed to the fact that DR and PR were adsorbed as liquids in experiments but treated as gases in simulation, meaning the rate of mass transfer was faster than that in the experiments.

This study can guide the separation of tetratoluene isomers in C_{10} heavy aromatics.

Supplementary Materials: The following supporting information can be downloaded at: https://www.mdpi.com/article/10.3390/pr12112331/s1, Figure S1: Optimized Structures of MOFs; Figure S2: Optimized structures of tetratoluene; Figure S3: The snapshot of four synthesized MOFs; Figure S4: The pore size distribution of four MOFs; Table S1: Atomic charges of DR and PR; Table S2: Adsorption capacity of DR and PR from 10 kPa to 300 kPa.

Author Contributions: T.W.: planning and execution of experiment, data analysis, writing—original draft. Y.W.: planning of experiment, writing—review and editing, supervision. J.R.: execution of experiment, data analysis. X.W.: execution of experiment, data analysis. B.W.: writing—review and editing. K.C.: writing—review and editing. L.J.: writing—review and editing. All authors have read and agreed to the published version of the manuscript.

Funding: This research received no external funding.

Data Availability Statement: The original contributions presented in the study are included in the article/supplementary material, further inquiries can be directed to the corresponding author.

Conflicts of Interest: The authors declare that they have no known competing financial interests or personal relationships that could have appeared to influence the work reported in this paper.

References

1. Oh, J.; Choi, Y.; Shin, J.; Kim, K.; Lee, J.K. Synergistic shape selectivity of H-Beta and H-ZSM-5 for Xylene-rich BTX production by hydrocracking of heavy-aromatic compounds. *Fuel Process. Technol.* **2023**, *249*, 107856. [CrossRef]
2. Goncalves, J.C.; Ferreira, A.F.P.; Rodrigues, A.E. Minimum Cross Diameter for C_6–C_{10} Aromatic Compounds. *Chem. Eng. Technol.* **2019**, *42*, 1169–1173. [CrossRef]
3. Ke, D.; Wang, M.J.; Ruan, J.C.; Chen, X.Z.; Zhou, S.D. Efficient, continuous oxidation of durene to pyromellitic dianhydride mediated by a V-Ti-P ternary catalyst: The remarkable doping effect. *Chinese J. Chem. Eng.* **2023**, *55*, 156–164. [CrossRef]
4. Li, M.Z.; Jiao, L.K.; Nawaz, M.A.; Cheng, L.K.; Meng, C.; Yang, T.H.; Tariq, M.; Liu, D.H. A one-step synthesis method of durene directly from syngas using integrated catalyst of Cu/ZnO/Al_2O_3 and Co-Nb/HZSM-5. Chem. *Eng. Sci.* **2019**, *200*, 103–112. [CrossRef]
5. Wang, Z.H.; Li, S.S.; Chen, C.H.; Jiang, Q.S.; Liu, D.H. Efficient synthesis of durene from syngas utilizing composite catalyst of Zr/Al activity-regulated CuZn oxides and alkali-treated HZSM-5-PEG. *Fuel* **2024**, *378*, 132800. [CrossRef]

6. Lai, Y.J.; Hong, B.; Zhou, W.; Wen, D.L.; Xie, Y.F.; Luo, F.; Ye, L.M.; Zuo, J.C.; Yuan, Y.Z. Upgrading Trimethylbenzene to Durene by CO_2-Mediated Methylation over Cu-Boosted $ZnZrO_x$ Integrated with HZSM-5. *ACS Catal.* **2024**, *14*, 11780–11793. [CrossRef]
7. Hayek, A.; Yahaya, G.O.; Alsamah, A.; Alghannam, A.A.; Jutaily, S.A.; Mokhtari, I. Pure-and sour mixed-gas transport properties of 4,4′-methylenebis(2,6-diethylaniline)-based copolyimide membranes. *Polymer* **2019**, *166*, 184–195. [CrossRef]
8. Li, G.Z.; Si, A.H.; Zhuang, Y.; Pang, S.Y.; Cui, Y.H.; Baeyens, J.; Qin, P.Y. A defects-free ZIF-90/6FDA-Durene membrane based on the hydrogen bonding/covalent bonding interaction for gas separation. *J. Membr. Sci.* **2022**, *661*, 120910. [CrossRef]
9. Yu, S.; Lim, C.S.; Seo, B. Tuning the free volume of polynorbornene-based membranes by blending 6FDA-durene to improve H_2 permselectivity. *J. Ind. Eng. Chem.* **2018**, *62*, 197–208. [CrossRef]
10. Hossain, I.; Al Munsur, A.; Kim, T.H. A Facile Synthesis of (PIM-Polyimide)-(6FDA-Durene-Polyimide) Copolymer as Novel Polymer Membranes for CO_2 Separation. *Membranes* **2019**, *9*, 113. [CrossRef]
11. Jusoh, N.; Yeong, Y.F.; Lau, K.K.; Shariff, A.M. Enhanced gas separation performance using mixed matrix membranes containing zeolite T and 6FDA-durene polyimide. *J. Membr. Sci.* **2017**, *525*, 175–186. [CrossRef]
12. Lyu, Q.M.; Cai, Y.F.; Wang, S.L.; Sun, W.Z.; Zhao, L. Experiments and Kinetic Modeling on the Co/Mn/Br Catalyzed Oxidation of Prehnitene to Mellophanic Acid in the Liquid Phase. *Ind. Eng. Chem. Res.* **2020**, *59*, 19226–19234. [CrossRef]
13. Merkelbach, J.; Frank, W. Synthesis, detailed geometric analysis and bond-valence method evaluation of the strength of pi-arene bonding of two isotypic cationic prehnitene tin(II) complexes: $[\{1,2,3,4\text{-}(CH_3)_4C_6H_2\}_2Sn_2Cl_2]$ $[MCl_4]_2$ (M = Al and Ga). *Acta Crystallogr. Sect. E Crystallogr. Commun.* **2019**, *75*, 1051–1056. [CrossRef]
14. Lyu, Q.M.; Sun, W.Z.; Zhao, L. Thermodynamic analysis and kinetic simulation of liquid phase oxidation of prehnitene to mellophanic acid. *CIESC J.* **2021**, *72*, 1009–1017. [CrossRef]
15. Ma, L.; Hou, M.; Wang, Y.M.; Tong, W.Y.; Zheng, J.L. Organosiloxane membranes for heavy aromatic oil fractionation. *Chem. Commun.* **2024**, *60*, 8083–8086. [CrossRef]
16. Guan, Y. Domestic and Foreign C_{10} Comprehensive Utilization Technology and Development trend. *Chem. Ind.* **2017**, *35*, 32–37. [CrossRef]
17. Mao, X.X.; Wu, Y.Y.; Zhang, X.C.; Cai, Y.Q.; Wu, B.; Chen, K.; Ji, L.J. Separation of durene and prehnitene by metal-organic framework UIO-66. Colloids Surf. A: Physicochem. *Eng. Asp.* **2022**, *641*, 127904. [CrossRef]
18. Shiau, L.D. Purification of durene from the mixture of durene and isodurene by stripping crystallization. *Korean J. Chem. Eng.* **2021**, *38*, 2510–2518. [CrossRef]
19. Wen, D.L.; Zuo, J.C.; Han, X.Q.; Liu, J.; Ye, L.M.; Yuan, Y.Z. Synthesis of durene by methylation of 1,2,4-trimethylbenzene with syngas over bifunctional $CuZnZrO_x$-HZSM-5 catalysts. *Catal. Sci. Technol.* **2022**, *12*, 2555–2565. [CrossRef]
20. Ren, H.; Yang, W.; Zhang, B. Opportunities for separation and utilization of C_9^+ heavy aromatics from reformation in China. *Mod. Chem. Ind.* **2020**, *40*, 11–14. [CrossRef]
21. Cong, S.; Liu, Y.; Li, H.; Li, X.G.; Zhang, L.H.; Wang, L. Purification and separation of durene by static melt crystallization. *Chin. J. Chem. Eng.* **2015**, *23*, 505–509. [CrossRef]
22. Zhu, M.H.; Liu, Y.D.; Wang, L.T.; Huang, Z.B.; Yuan, P.Q. Selective extraction of aromatics from residual oil with subcritical water. *Chem. Eng. Res. Des.* **2024**, *202*, 444–454. [CrossRef]
23. Li, J. Production Technology and Industry Progress Research of 1,2,4,5-Tetramethylbenzene. *Shandong Chem. Ind.* **2023**, *52*, 113–115. [CrossRef]
24. Li, X.G.; Liu, Y.; Li, H.; Cong, S.; Xu, C.; Wang, L. Purification of by-product durene in methanol synthetic oil by crystallization. *Chem. Eng.* **2013**, *41*, 14–18.
25. Jusoh, N.; Yeong, Y.F.; Cheong, W.L.; Lau, K.K.; Shariff, A.M. Facile fabrication of mixed matrix membranes containing 6FDA-durene polyimide and ZIF-8 nanofillers for CO_2 capture Petrochemical Technology. *J. Ind. Eng. Chem.* **2016**, *44*, 164–173. [CrossRef]
26. Rezki, M.; Septinai, N.L.W.; Iqbal, M.; Adhika, D.R.; Wenten, I.G.; Yuliarto, B. Review-Recent Advance in Multi-Metallic Metal Organic Frameworks(MM-MOFs) and Their Derivatives for Electrochemical Biosensor Application. *J. Electrochem. Soc.* **2022**, *169*, 017504. [CrossRef]
27. Zhang, W.Q.; Li, X.J.; Ding, X.M.; Hua, K.; Sun, A.L.; Hu, X.X.; Nie, Z.W.; Zhang, Y.S.; Wang, J.C.; Li, R.L.; et al. Progress and opportunities for metal-organic framework composites in electrochemical sensors. *RSC Adv.* **2023**, *13*, 10800–10817. [CrossRef]
28. Kulak, H.; Polat, H.M.; Kavak, S.; Keskin, S.; Uzun, A. Improving CO_2 Separation performance of MIL-53(Al) by incorporating 1-n-butyl-3-methylimidazolium methyl sulfate. *Energy Technol.* **2019**, *7*, 1900157. [CrossRef]
29. Sun, Y.X.; Jia, X.; Huang, H.L.; Guo, X.Y.; Qiao, Z.H.; Zhong, C.L. Solvent-free mechanochemical route for the construction of ionic liquid and mixed-metal MOF composites for synergistic CO_2 fixation. *J. Mater. Chem. A* **2020**, *8*, 3180–3185. [CrossRef]
30. Skarmoutsos, I.; Eddaoudi, M.; Maurin, G. Highly tunable sulfur hexafluoride separation by interpenetration control in metal organic frameworks. *Microporous Mesoporous Mater.* **2019**, *281*, 44–49. [CrossRef]
31. Li, J.; Wang, X.X.; Zhao, G.X.; Chen, C.L.; Chai, Z.F.; Alsaedi, A.; Hayat, T.; Wang, X.K. Metal-organic framework-based materials superior adsorbents for the capture of toxic and radioactive metal ions. *Chem. Soc. Rev.* **2018**, *47*, 2322–2356. [CrossRef] [PubMed]
32. Konneryh, H.; Matsagar, B.M.; Chen, S.S.; Prechtl, M.H.G.; Shieh, F.K.; Wu, K.C.W. Metal-organic framework(MOF) derived catalysts for fine chemical production. *Coordin. Chem. Rev.* **2020**, *416*, 213319. [CrossRef]

33. Jiang, J.X.; Shi, Y.; Wu, M.J.; Rezakazemi, M.; Aminabhavi, T.M.; Huang, R.Z.; Jia, C.; Ge, S.B. Biomass-MOF composites in wastewater treatment, air purification, and electromagnetic radiation adsorption—A review. *Chem. Eng. J.* **2024**, *494*, 152932. [CrossRef]
34. Liu, C.; Qiao, J.; Zhang, X.; Xu, D.M.; Wu, N.N.; Lv, L.F.; Liu, W.; Liu, J.R. Bimetallic MOF-derived porous CoNi/C nanocomposites with ultra-wide band microwave absorption properties. *New J. Chem.* **2019**, *43*, 16546–16554. [CrossRef]
35. Zhao, Y.J.; Zhao, H.F.; Liu, D.H. Selective Adsorption and Separation of o-Xylene Using an Aluminum-Based Metal-Organic Framework. *Ind. Eng. Chem. Res.* **2021**, *60*, 17143–17149. [CrossRef]
36. He, Z.J.; Yang, Y.X.; Bai, P.; Guo, X.H. Metal-organic framework MIL-53(Cr) as a superior adsorbent: Highly 8 efficient separation of xylene isomers in liquid phase. *J. Ind. Eng. Chem.* **2019**, *77*, 262–272. [CrossRef]
37. Bae, H.J.; Kim, S.I.; Choi, Y.; Kim, K.M.; Bae, Y.S. High p-xylene selectivity in aluminum-based metal-organic framework with 1-D channels. *J. Ind. Eng. Chem.* **2023**, *117*, 333–341. [CrossRef]
38. Lin, Y.H.; Zhang, J.; Pandey, H.; Dong, X.L.; Gong, Q.H.; Wang, H.; Yu, L.; Zhou, K.; Yu, W.; Huang, X.X.; et al. Efficient separation of xylene isomers by using a robust calcium-based metal-organic framework through a synergetic thermodynamically and kinetically controlled mechanism. *J. Mater. Chem. A.* **2021**, *9*, 26202–26207. [CrossRef]
39. Yang, L.P.; Liu, H.B.; Yuan, D.H.; Xing, J.C.; Xu, Y.P.; Liu, Z.M. Efficient Separation of Xylene Isomers by a Pillar-Layer Metal-Organic Framework. *ACS Appl. Mater. Interfaces* **2021**, *13*, 41600–41608. [CrossRef]
40. Feng, L.; Liu, J.J.; Abu-Hamdeh, N.H.; Bezzina, S.; Malekshah, R.E. Molecular dynamics and quantum simulation of different cationic dyes removal from contaminated water using UiO-66-$(COOH)_2$ metal-organic framework. *J. Mol. Liq.* **2022**, *349*, 118085. [CrossRef]
41. Kim, S.I.; Lee, S.; Chung, Y.G.; Bae, Y.S. The Origin of p-Xylene Selectivity in a DABCO Pillar-Layered Metal-Organic Framework: A Combined Experimental and Computational Investigation. *ACS Appl. Mater. Interfaces* **2019**, *11*, 31227–31236. [CrossRef] [PubMed]
42. Ji, G.J.; Xiang, T.; Zhou, X.Q.; Chen, L.; Zhang, Z.H.; Lu, B.B.; Zhou, X.J. Molecular dynamics simulation of adsorption and separation of xylene isomers by Cu-HKUST-1. *RSC Adv.* **2022**, *12*, 35290–35299. [CrossRef] [PubMed]
43. Wang, V.; Xu, N.; Liu, J.C.; Tang, G.; Geng, W.T. VASPKIT: A user-friendly interface facilitating high-throughput computing and analysis using VASP code. *Comput. Phys. Commun.* **2021**, *267*, 108033. [CrossRef]
44. Sun, A.Q.; Wu, Y.; He, Z.J.; Bai, P.; Lyu, J.F.; Guo, X.H. Manipulated adsorption of C_8 aromatics in MIL-53(Cr) through pre-adsorbing water molecules. *J. Taiwan Inst. Chem. E* **2021**, *122*, 222–230. [CrossRef]
45. Chen, K.M.; Liu, P.X.; Wang, Y.; Ren, Y.H.; Liu, J.H.; Chen, Y.; Li, J.P.; Li, L.B. Structural functionalization in robust metal-organic frameworks for p-xylene separation with superior adsorption capacity. *Microporous Mesoporous Mater.* **2023**, *360*, 112705. [CrossRef]
46. Ribeiro, R.P.P.L.; Mota, J.P.B. Surface Area and Porosity of $Co_3(ndc)_3(dabco)$ Metal-Organic Framework and Its Methane Storage Capacity: A Combined Experimental and Simulation Study. *J. Phys. Chem. C* **2021**, *125*, 2411–2423. [CrossRef]
47. Xu, Z.W.; Ni, K.Y.; Mao, J.M.; Luo, T.K.; Lin, W.B. Monte Carlo Simulations Reveal New Design Principles for Efficient Nanoradiosensitizers Based on Nanoscale Metal-Organic Frameworks. *Adv. Mater.* **2021**, *33*, 2104249. [CrossRef]
48. Yuvaraj, A.R.; Jayarama, A.; Sharma, D.; Nagarkar, S.S.; Duttagupta, S.P.; Pinto, R. Role of metal-organic framework in hydrogen gas storage: A critical review. *Int. J. Hydrogen. Energ.* **2024**, *59*, 1434–1458. [CrossRef]
49. Han, B.; Chakraborty, A. Tailoring Zirconium-based metal organic frameworks for enhancing Hydrophilic/Hydrophobic Characteristics: Simulation and experimental investigation. *J. Mol. Liq.* **2021**, *341*, 117381. [CrossRef]
50. Jing, B.Y.; Xia, D.; Wang, G.Q. Adsorption and Self-Diffusion of R32/R1234yf in MOF-200 Nanoparticles by Molecular Dynamics Simulation. *Processes* **2022**, *10*, 1714. [CrossRef]
51. Mao, M.; Wu, X.X.; Hu, Y.; Yuan, Q.H.; He, Y.B.; Kang, F.Y. Charge storage mechanism of MOF-derived Mn_2O_3 as high performance cathode of aqueous zinc-ion batteries. *J. Energy Chem.* **2021**, *52*, 277–283. [CrossRef]
52. Vo, T.K.; Bae, Y.S.; Chang, B.J.; Moon, S.Y.; Kim, J.H.; Kim, J. Highly CO Selective Cu(I)-Doped MIL-100(Fe) Adsorbent with High CO/CO_2 Selectivity due to π Complexation: Effects of Cu(I) Loading and Activation Temperature. *Microporous Mesoporous Mater.* **2019**, *274*, 17–24. [CrossRef]
53. Zhang, Y.Y.; Hu, G.F.; Gao, X.T.; Zhang, Z.X.; Cui, P. Simulation study on functional group-modified Ni-MOF-74 for CH_4/N_2 adsorption separation. *J. Comp. Chem.* **2024**, *45*, 1515–1524. [CrossRef]
54. Chen, Y.B.; Tang, J.L.; Wang, S.X.; Zhang, L.B. Facile preparation of a remarkable MOF adsorbent for Au(III) selective separation from wastewater: Adsorption, regeneration and mechanism. *J. Mol. Liq.* **2022**, *349*, 118137. [CrossRef]
55. Li, Y.; Lin, H.; Yu, Q.L.; Ma, N.; Dai, W. UiO-66-NH_2 nanoparticles supported on layered double hydroxides as an excellent adsorbent for levofloxacin capture. *Particuology* **2024**, *92*, 155–165. [CrossRef]
56. Li, Y.J.; Cui, J.Y.; Wang, Q.J.; Yang, L.F.; Chen, L.Y.; Xing, H.B.; Cui, X.L. Responsive shape recognition of styrene over ethylbenzene with excellent selectivity and capacity in a hybrid porous material. *Chem. Eng. J.* **2023**, *453*, 139456. [CrossRef]
57. Zhou, J.W.; Liu, M.; Chen, X.; Bai, S.Y.; Sun, J.H. Interfacial growth strategy for synthesizing Mg-MOF-74@clinoptilolites with hierarchical structures for enhancing adsorptive separation performance of CO_2/CH_4, CH_4/N_2 and CO_2/N_2. *Surf. Interfaces* **2024**, *54*, 105106. [CrossRef]
58. Li, L.C.; Xu, Y.L.; Zhong, D.J.; Zhong, N.B. CTAB-surface-functionalized magnetic MOF@MOF composite adsorbent for Cr(VI) efficient removal from aqueous solution. *Colloids Surf. A Physicochem. Eng. Asp.* **2020**, *586*, 124255. [CrossRef]

59. Yu, K.; Ahmed, I.; Wong, D.I.; Lee, W.I.; Ahn, W.S. Highly efficient adsorptive removal of sulfamethoxazole from aqueous solutions by porphyrinic MOF-525 and MOF-545. *Chemosphere* **2020**, *250*, 126133. [CrossRef] [PubMed]
60. Wu, H.; Zhou, W.; Yildirim, T. High-Capacity Methane Storage in Metal−Organic Frameworks M_2(dhtp): The Important Role of Open Metal Sites. *J. Am. Chem. Soc.* **2009**, *131*, 4995–5000. [CrossRef]
61. Chen, S.; Li, Y.J.; Yang, L.F.; Zhang, X.M.; Yang, Z.L.; Zhou, L.; Cui, X.L.; Xing, H.B. Anion-pillared porous materials with suitable pore size for the efficient discrimination of cyclohexene from cyclohexane. *Sep. Purif. Technol.* **2022**, *302*, 122095. [CrossRef]
62. Li, T.; Cheng, C.X.; Zhang, K.F.; Yang, J.; Han, G.S.; Wang, X.J.; Wang, Z.P.; Wang, L.G. UiO-66-NH_2 nanocomposites incorporated cellulose acetate for forward osmosis membranes of high desalination performance. *Environ. Technol.* **2024**, *45*, 16–27. [CrossRef] [PubMed]
63. Yu, Z.Z.; Anstine, D.M.; Boulfelfel, S.E.; Gu, C.K.; Colina, C.M.; Sholl, D.S. Incorporating Flexibility Effects into Metal-Organic Framework Adsorption Simulations Using Different Models. *ACS Appl. Mater. Interfaces* **2021**, *13*, 61305–61315. [CrossRef] [PubMed]
64. Yeganegi, S.; Gholami, M.; Sokhanvaran, V. Molecular simulations of adsorption and separation of acetylene and methane and their binary mixture on MOF-5, HKUST-1 and MOF-505 metal-organic frameworks. *Mol. Sim.* **2017**, *43*, 260–266. [CrossRef]
65. Chen, B.; Li, Y.H.; Li, M.X.; Cui, M.F.; Xu, W.S.; Li, L.B.; Sun, Y.H.; Wang, M.Z.; Zhang, Y.; Chen, K.W. Rapid adsorption of tetracycline in aqueous solution by using MOF-525/graphene oxide composite. *Microporous Mesoporous Mater.* **2021**, *328*, 111457. [CrossRef]
66. Cui, X.L.; Niu, Z.; Shan, C.; Yang, L.F.; Hu, J.B.; Wang, Q.J.; Lan, P.C.; Li, Y.J.; Wojtas, L.; Ma, S.Q.; et al. Efficient separation of xylene isomers by a guest-responsive metal-organic framework with rotational anionic sites. *Nat. Commun.* **2020**, *11*, 5456. [CrossRef]
67. Bai, Y.H.; Chen, H.H.; Cheng, H.; Ding, Z.X.; Yuan, R.S.; Li, Z.H. Coupling physical adsorption and photocatalysis over CdS/UiO-66-NH_2 for efficient removal of hydrogen sulfide. *Sep. Purif. Technol.* **2024**, *341*, 126956. [CrossRef]
68. Kyriakopoulos, G.; Xiarchos, I.; Doulia, D. Treatment of contaminated water with pesticides via adsorption. *Int. J. Environ. Technol. Manag.* **2006**, *6*, 515–524. [CrossRef]
69. Song, W.H.; Yao, J.; Ma, J.S.; Li, A.F.; Li, Y.; Sun, H.; Zhang, L. Grand canonical Monte Carlo simulations of pore structure influence on methane adsorption in micro-porous carbons with applications to coal and shale systems. *Fuel* **2018**, *215*, 196–203. [CrossRef]
70. Frank, H.O.; Paesani, F. Molecular driving forces for water adsorption in MOF-808: A comparative analysis with UiO-66. *J. Chem. Phys.* **2024**, *160*, 094703. [CrossRef]

Disclaimer/Publisher's Note: The statements, opinions and data contained in all publications are solely those of the individual author(s) and contributor(s) and not of MDPI and/or the editor(s). MDPI and/or the editor(s) disclaim responsibility for any injury to people or property resulting from any ideas, methods, instructions or products referred to in the content.